ISCI, Volume *19*

Supplemental Information

Anisotropic Singlet Fission in Single Crystalline Hexacene

Dezheng Sun, Gang-Hua Deng, Bolei Xu, Enshi Xu, Xia Li, Yajing Wu, Yuqin Qian, Yu Zhong, Colin Nuckolls, Avetik R. Harutyunyan, Hai-Lung Dai, Gugang Chen, Hanning Chen, and Yi Rao

Supplemental Information

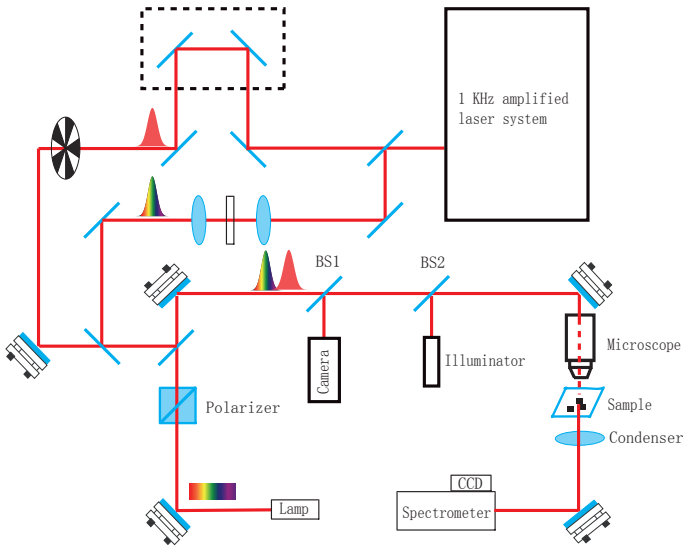

Figure S1. Schematic diagram of transient absorption setup coupled with home-built microscope. Related to Figure 1.

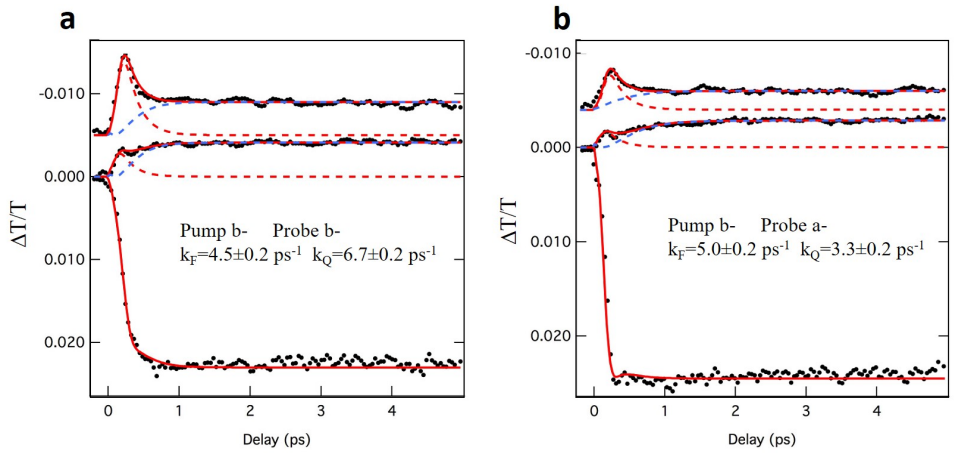

Figure S2. Global Fittings of kinetics traces with probes along ***b*** (left) and ***a*** (right) axes when the photoexcitation is applied along ***b*** axis. The dynamics has been shift vertically for clearance. The solid red line and blue line are fitted curve while the black dots are the raw data. The colored dashed lines correspond to singlet component (red) and triplet component (blue) based on the fitting results. Related to Figure 4.

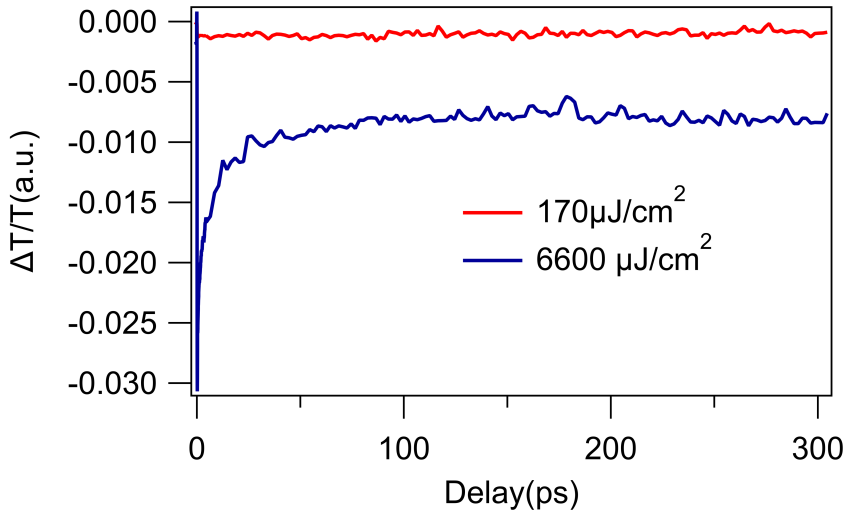

Figure S3 Triplet Exciton-Exciton Annihilation. Measured pump-induced signal of triplet state along b-axis at low (170μJ/cm^2) and high (6600μJ/cm^2) pump influence. The pump beam was set at 795 nm. The polarization of the pump beam was set along b-axis of the hexacene single crystal. Related to Figure 3.

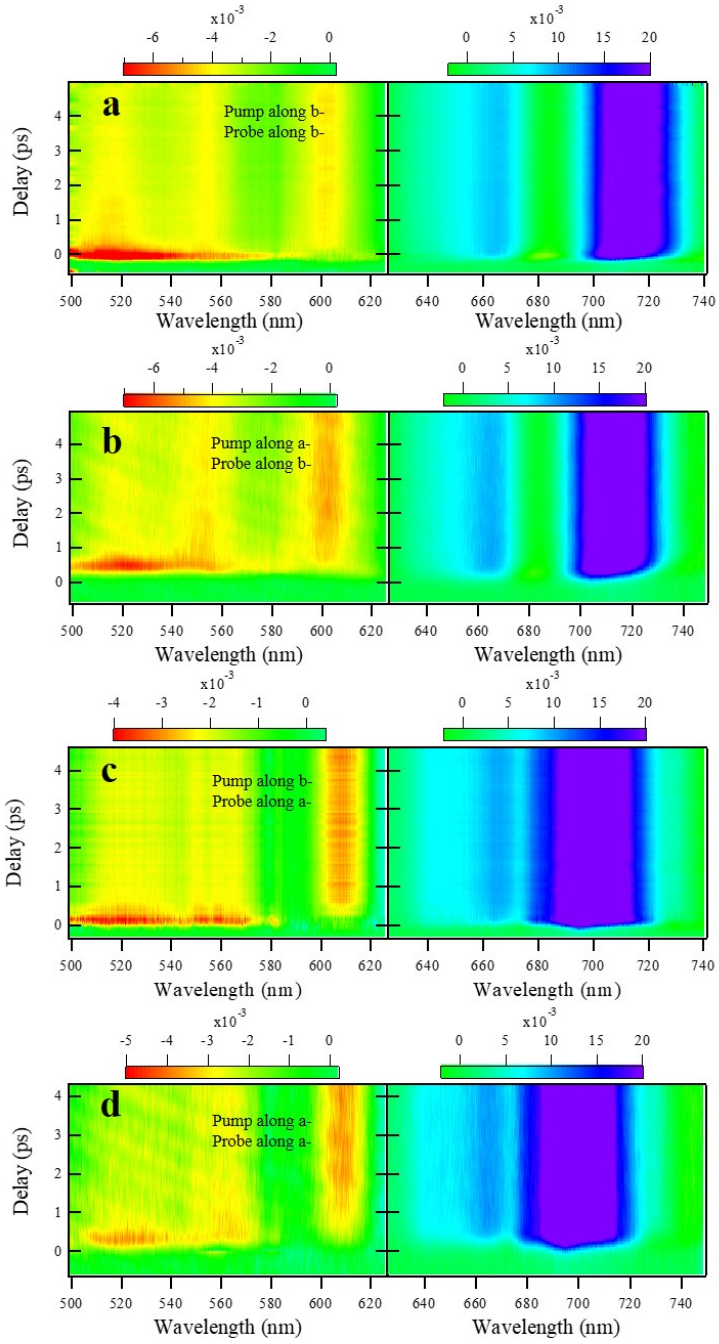

Figure S4 Comparison of transient spectra between all four possible polarization combinations: (a) ***b***-axis pump / ***b***-axis probe, (b) ***a***-axis pump / ***b***-axis probe, (c) ***b***-axis pump / ***a***-axis probe, (d) ***a***-axis pump / ***a***-axis probe. The transient responses of hexacene single crystals strongly depend on the probe polarization, whereas they are independent of the pump polarization. Related to Figure 3.

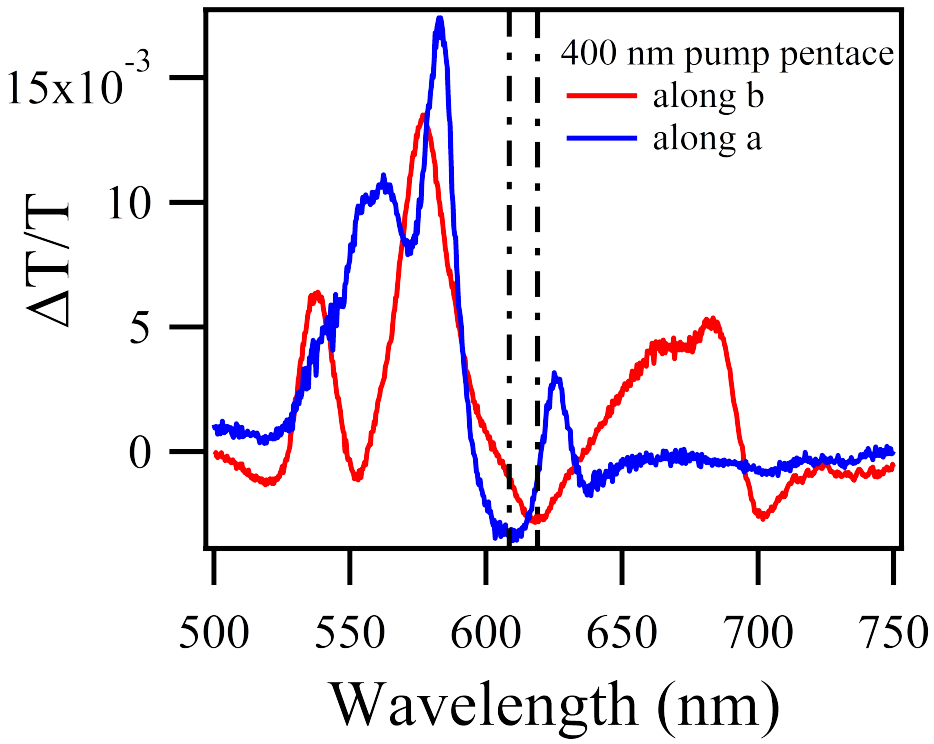

Figure S5. Transient absorption spectra of pentacene single crystals at a time delay of 4 ps probing along the long *a*- axis and short *b*-axis when a 400-nm photoexcitation is applied along the *b*-axis. The $T_1 \rightarrow T_n$ transitions exhibit different absorption peaks at 609 nm and 619 nm along the long *a*-axis and short *b*-axis, respectively. Related to Figure 3.

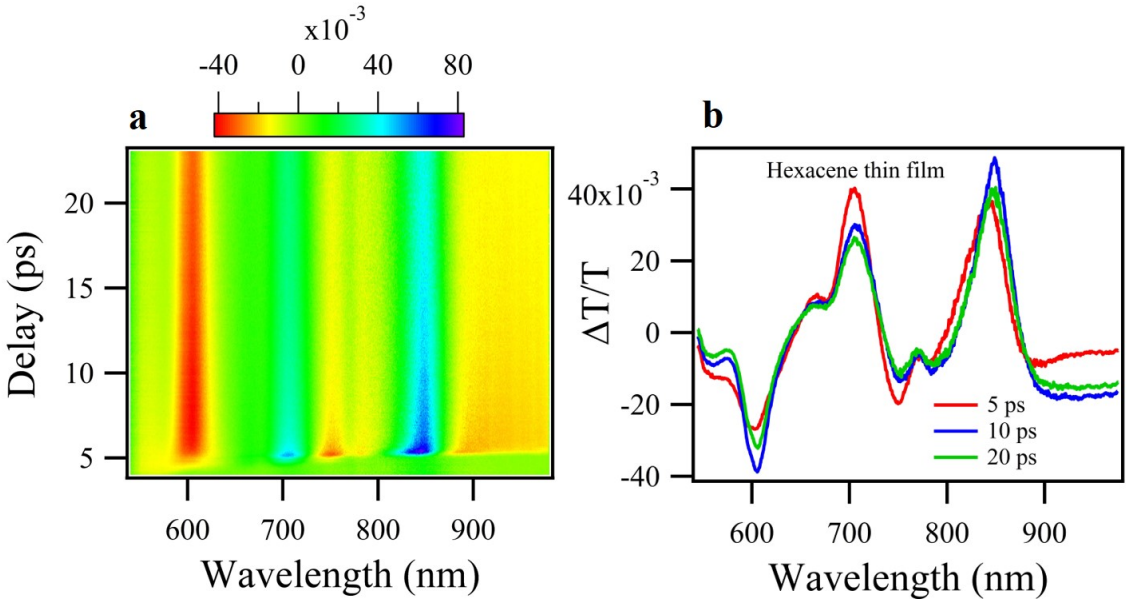

Figure S6. Singlet Fission in Hexacene Thin Film under 515 nm Photoexcitation. (a) Pseudo-color plots of transient absorption spectra from hexacene thin film excited at 515 nm. (b) Transient absorption spectra of hexacene thin film at times delay of 5, 10 and 15 ps. Related to Figure 3.

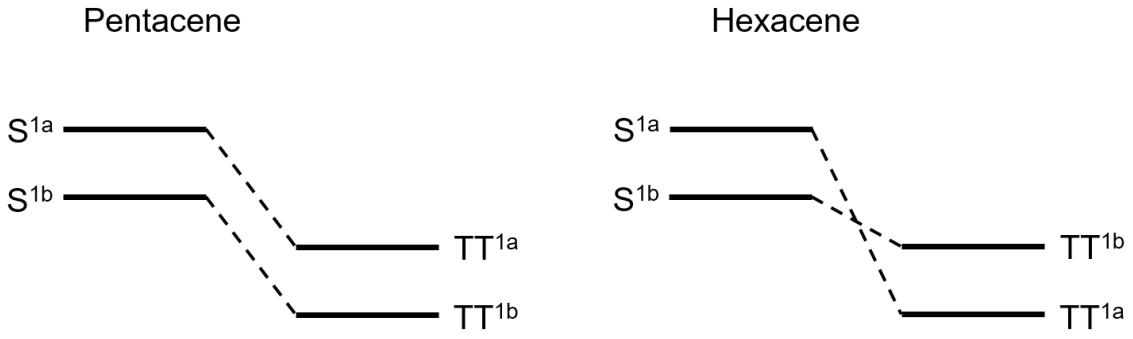

Figure S7 Energy diagram of singlet Davydov splitting and triplet Davydov splitting of pentacene and haxacene. Related to Figure 2.

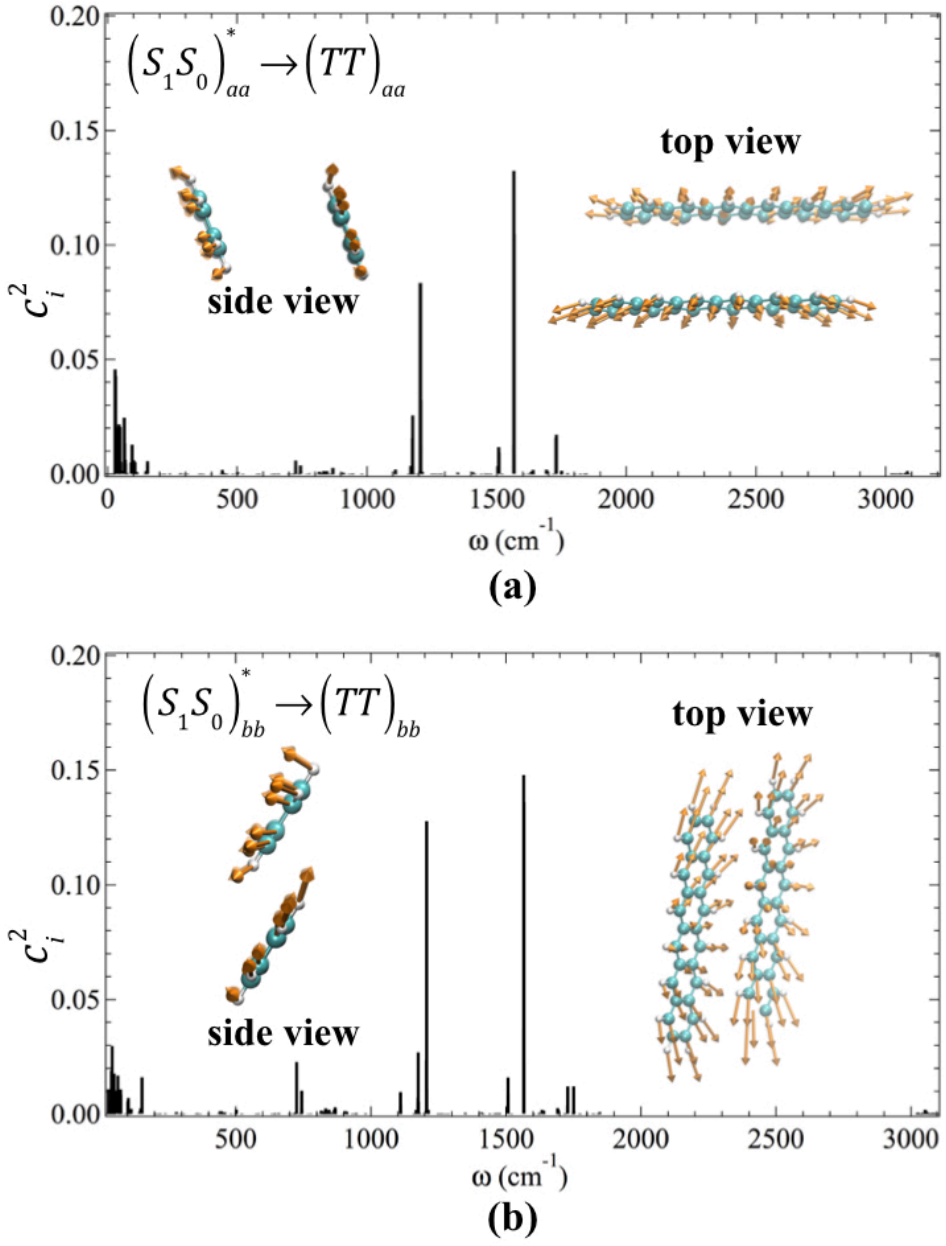

Figure S8. Calculated driving vibrational modes, $\vec{V}_{SF} = \sum_i c_i \vec{V}_i$, for singlet fission within an adjacent hexacene molecules along axes a and b. Their constituents in terms of c_i^2 are also presented alongside their side and top views. For visual clearance, only the displacement vectors on the participating molecules of singlet-fission are displayed. Related to Scheme 1.

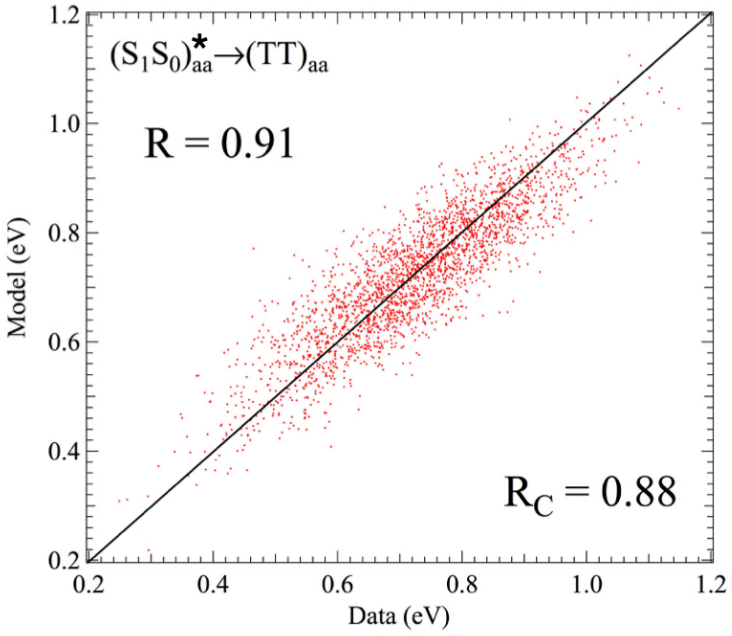

(a)

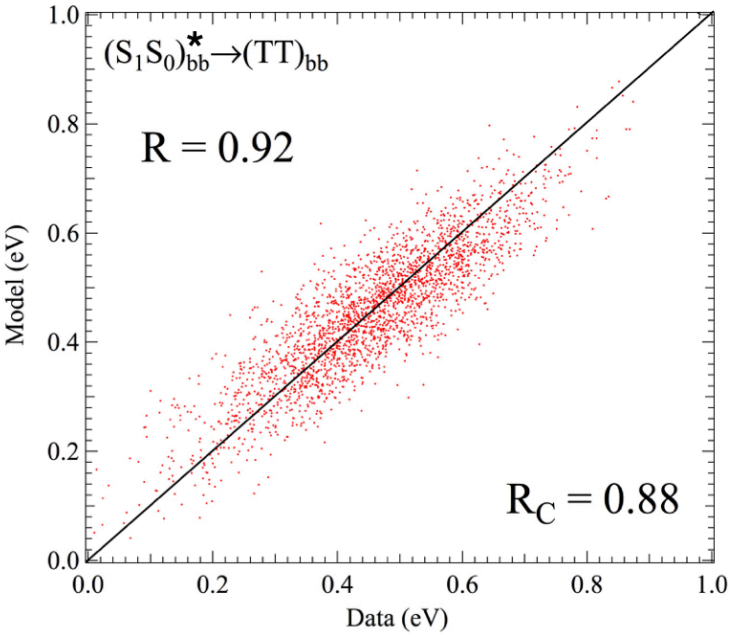

(b)

Figure S9. Scatter plots for the cross validation of $\vec{V}_{SF}$ along ***a*** and ***b*** axes. Related to Scheme 1.

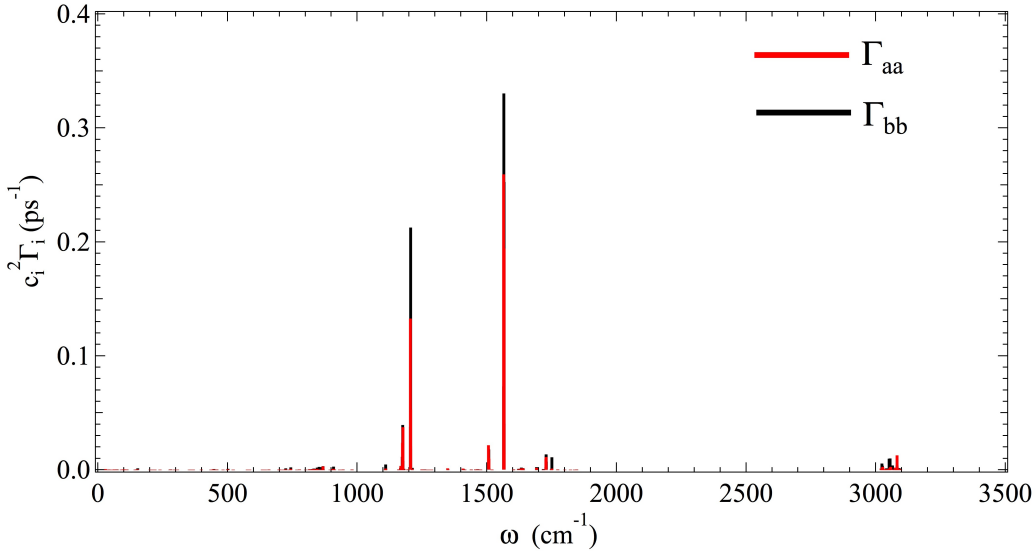

Figure S10. Profile of the thermal relaxation rate, Γ_i, of vibrational normal modes weighted by their relative importance, c_i^2, to the singlet-fission driving mode, $\vec{V}_{SF}$. Related to Scheme 1.

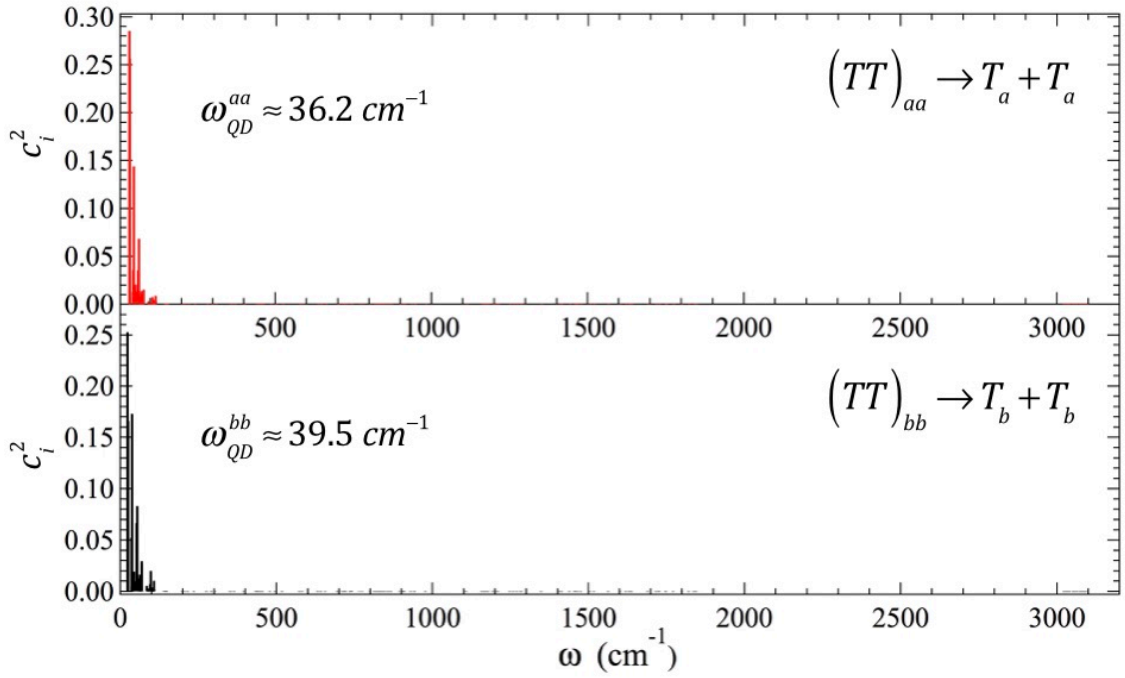

Figure S11. Components of the vibrational modes that drive quantum decoherence to decouple TT into $T+T$ along ***a*** and ***b*** axes. Related to Scheme 1.

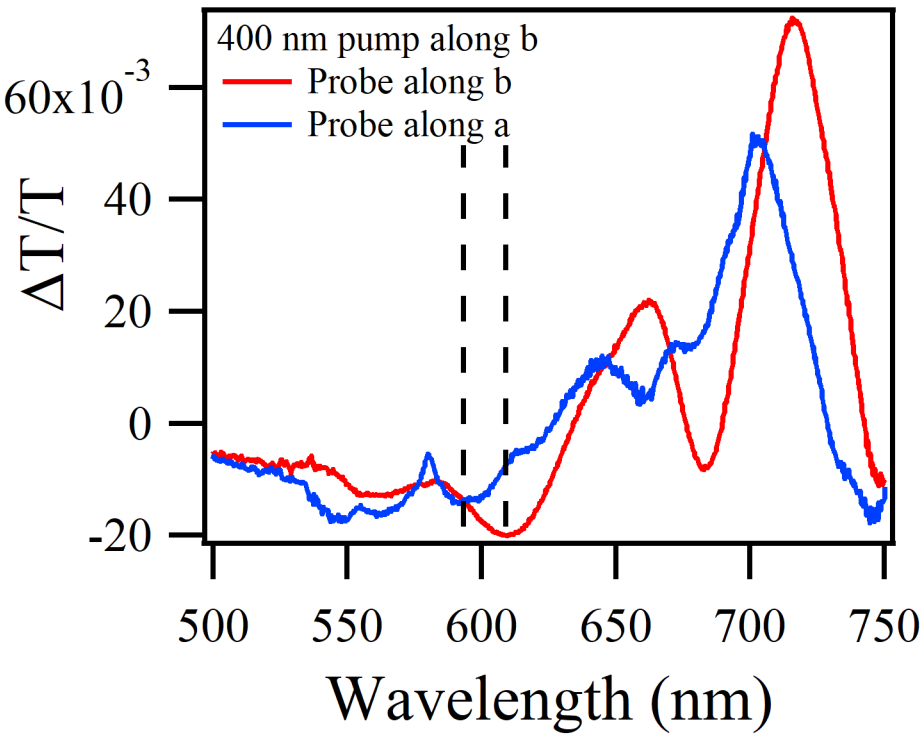

Figure S12. Transient absorption spectra of hexacene single crystals at a time delay of 6.4 ps probing along the long a- axis and short b-axis when a 400-nm photoexcitation is applied along the b-axis. The $T_1 \rightarrow T_n$ transitions exhibit different absorption peaks at 594 nm and 610 nm along the long a- axis and short b-axis, respectively. Related to Figure 3.

Supplemental Tables

Table S1. The energy gaps and oscillator strengths of the $S_0S_0 \rightarrow S_1S_0^*$ optical transitions along the ***a*** and ***b*** axes, alongside their projected transition dipole moments. Related to Figure 2.

lattice direction	aa	bb
$\Delta E\left(S_0S_0 \rightarrow S_1S_0^*\right)\left(eV\right)$	1.65	1.42
$f_{12}\left(10^{-3}\right)$	5.57	8.94
$D_a\left(debye\right)$	0.82	0.04
$D_b\left(debye\right)$	0.39	1.13
$D_c\left(debye\right)$	0.03	0.06

Table S2. Key parameters for the $S_0S_1 \rightarrow (TT)$ transition rate along axes a and b. ΔG_0 is the driving force, λ is the reorganization energy, J is the electronic coupling strength, Ω is the effective angular frequency of the driving vibrational mode, Γ is its thermal relaxation rate, k_F is the singlet fission rate, and k_D is the decay rate of S_0S_1. Related to Figure 4.

lattice direction	aa	bb
$\Delta G_0(eV)$	-0.62	-0.43
$\lambda(eV)$	0.46	0.40
$J(meV)$	9.2	10.9
$\Omega(cm^{-1})$	1752	1901
$\Gamma(ps^{-1})$	0.93	1.25
$k_F(ps^{-1})$	0.93	0.83
$k_D(ps^{-1})$	1.86	2.08

Table S3. Key parameters for the quantum decoherence rates, k_Q, along ***a*** and ***b*** axes according to the Redfield theory. Related to Figure 4 and Scheme 1.

lattice direction	aa	bb
$\Delta E_{QD}\ (meV)$	42	26
$\lambda\ (meV)$	8	6
$\omega_p\left(cm^{-1}\right)$	36.2	39.5
$k_Q\left(ps^{-1}\right)$	3.2	5.3

Transparent Methods

Preparation of Single Crystals

Hexacene single crystals were grown in a physical vapor transport (PVT) furnace at atmospheric pressure. Hexacene precursor was synthesized according to a previously reported method(Laudise et al., 1998; Watanabe et al., 2012). ~1 mg hexacene powder was heated in a hot zone of the furnace at 300 °C for a week. 50 SCCM of ultrahigh purity argon gas (99.999%) was used as purging gas as well as carrier gas. Hexacene single crystals were collected in the crystallization zone. Single crystals grown in this manner were first spread on a quartz substrate. The hexacene crystal face for this method tends to grow parallel to the substrate, namely (001). A gasket sealed container to hold the quartz substrate was assembled in the N_2 box to protect the single crystals from oxygen during optical experiments.

Experimental Setup for Micro Transmission UV-vis Spectrometer

The optical absorption measurements of hexacene single crystals were performed on a home-built microscope equipped with a lamp (Lumina-I) as an unpolarized broadband radiation source. Briefly, an intensity-tunable halogen-lamp and a LED pen light were used as the UV-vis light source for the UV-vis transmission measurements and the illumination light for the microscope, respectively. A beam splitter combined both the UV-vis and illumination light for a collinear light path. An objective with 10× magnification subsequently focused the selected polarized light onto a hexacene single crystal at normal incident angle. A condenser was used to collect the transmitted light that is turn was focused into a grating spectrometer (Andor Shamrock 500 with a grating blazed at 500nm, 150 groove/mm), followed by a thermo-cooled CCD (Andor Newton). A polarizer was placed between the lamp and the objective to select the polarization of the incident light. Only a few of crystallites met the requirements of the optical measurements on each substrate, even though small single crystals have been intentionally prepared. The thicknesses of the chosen hexacene samples were estimated to be on the order of ca. 0.5 μm according to the absorption coefficient of hexacene thin films reported in the literature. All experiments were performed at room temperature.

Micro-transient Absorption Spectrometer

A home-built microscope was coupled with a transient absorption setup for our micro-transient absorption measurements (Figure S1). We used 1 KHz regeneratively amplified Ti: Sapphire laser system to generate laser pulse with a center wavelength at 795 nm. The pulse duration is about 100 fs. The laser pulse was then split into two parts: one part was coupled with a motorized delay stage (Klinger) as a pump light, and the other part was focused onto a sapphire crystal plate to generate white light super-continuum as a probe light. Both the pump light and the probe light have been combined by a pellicle beam splitter and sent to the objective. Two more beam splitters were used along the beam path to couple the illumination light and a CMOS camera for imaging samples. The transmitted probe light was collected by a condenser and sent to the spectrometer and CCD (Andor Shamrock and Andor Newton, respectively). The pump light was blocked after passing the samples by placing an appropriate band pass filter. The time-dependent changes in absorption spectra have been obtained by switching on/off of the pump pulse. The CCD sampling rate of 200 Hz was synchronized with an optical chopper. A detection sensitivity of about 5×10^{-4} was achieved.

Estimation of Photo-excited Carrier Density for Singlet Fission

We estimated the photo-excited carrier density as follows:

1). We measured the transmission of the hexacene sample on quartz comparing with clean quartz substrate and observed approximately 20-fold decrease of the transmission light at 730 nm. By using a known extinction coefficient for hexacene single crystal at the same wavelength (0.25×10^5 cm^{-1}), we obtained the crystal thickness of about 520 nm.

$$I(z) = I(0) \cdot 10^{-\alpha(\lambda)z}$$
$$z = \log 20 / \alpha(\lambda) = 520\text{nm}$$

2). For 0.25 μW 795 nm femtosecond laser pulse, the number of photons per volume is given by

$$\frac{0.25\times10^{-6}}{10^{3}}\times\frac{3}{7}\times0.25\times10^{5}\,cm^{-1}\times0.52\times10^{4}\,cm\times$$
$$\frac{1}{\frac{1240}{795}\times1.6\times10^{-19}}\times\frac{1}{\pi\times(4.5\times10^{-4}\,cm)^{2}\times0.52\times10^{4}\,cm}$$
$$=2.1\times10^{19}\,cm^{-3}$$

3). If we assume that each absorbed photon generates one singlet exciton, the initial singlet exciton density is 2.1×10^{19} cm^{-3}.

4). Laser fluence:

$$\frac{Energy\,/\,pulse}{area}=\frac{0.25nJ/(7/3)}{\pi*(4.5\mu m)^{2}}=170\mu J/cm^{2}$$

5). Excitation volume:

$$\mathrm{V_{ext}}=\mathrm{Area}*\mathrm{Thickness}=\pi\cdot(4.5\mu\mathrm{m})^{2}\cdot0.52\mu\mathrm{m}=33\mu\mathrm{J/cm^{2}}$$

6). Volume of hexacene:

a=7.673Å, b=6.292Å, c=16.242Å

$$V=abc=784.13\ \mathrm{A}^{3}$$

Since there are two molecules in a unit cell, the volume of each molecule is 392.06 Å^3

7). The ratio of excited molecule density vs total molecule density:

$$\frac{\mathrm{D_{ext}}}{\mathrm{D_{tot}}}=\frac{2.1\times10^{19}\,\mathrm{cm^{-3}}}{1/392\mathrm{A}^{3}}=8.5\times10^{-3}$$

8). The expected pump probe signal without considering singlet fission:

$$\frac{\Delta\mathrm{T}}{\mathrm{T}}(\mathrm{S_0}-\mathrm{S_1})=\sigma(\mathrm{S_0})\times\mathrm{N}(\mathrm{S_1})=1.1\times10^{-2}$$

Coupled Rate Equations of Singlet Fission

$$S_0+S_1\xrightarrow{k_F}{}^{1}\left(T_1T_1\right)\xrightarrow{k_Q}T_1+T_1$$

k_F: the formation rate of a correlated triplet pair state

k_Q: the quantum decoherence rate of a correlated triplet pair state

By solving the two-step coupled rate equation, we can write the population dynamics for singlet and triplet exciton as

$$Singlet(\mathrm{t}) = \mathrm{A}_0\, e^{-k_F t}$$
$$TT(\mathrm{t}) = \frac{k_F\, \mathrm{A}_0}{k_F - k_Q}(e^{-k_F t} - e^{-k_Q t})$$
$$\mathrm{T}_1(\mathrm{t}) = \mathrm{A}_0(1 + \frac{1}{k_F - k_Q}(k_Q e^{-k_F t} - k_F e^{-k_Q t})) \qquad \text{Equation S1}$$

Global Fitting Based on Coupled Rate Equations for Singlet Fission

We noticed that all the kinetic traces include both the contributions from the $S_1 \rightarrow S_n$ and $T_1 \rightarrow T_n$ transitions. As such, we made our kinetic analyses by considering: 1) Transient responses at any energy are a sum of the $S_1 \rightarrow S_n$ and $T_1 \rightarrow T_n$ transitions; 2) Singlet fission is a two-step process with two independent rates, namely k_F and k_Q. The justification of the latter was based on the fact that the decay rate of S_1 is not consistent with the generation rate of T_1 from our kinetic data, in particular along the ***a*** axis. Specifically, we treat $\Delta T/T(E, t)$ as a sum of the contributions from both the S_1-S_n and T_1-T_n transitions at a given energy: $-\Delta T/T(E, t) = \sigma_{S1\text{-}Sn}(E) n_{S1}(t) + \sigma_{T1\text{-}Tn}(E) n_{T1}(t)$, where $n_{S1}(t)$ and $n_{T1}(t)$ are standard time-dependent populations of a two-step sequential reaction as given in Equation 1, and $\sigma_{S1\text{-}Sn}(E)$ and $\sigma_{T1\text{-}Tn}(E)$ are the cross sections for the $S_1 \rightarrow S_n$ and $T_1 \rightarrow T_n$ transitions.

Based on the kinetic model and the rate equations described above, we are able to apply the global fitting to our transient absorption data at different time delays. The change in measured transient transmission is proportional to the absorption cross section for each of the three following transitions: $S_0 \rightarrow S_1$, $S_1 \rightarrow S_n$ and $T_1 \rightarrow T_n$.

$$\begin{cases} \dfrac{\Delta T}{T}(S_1 - S_n) = -\sigma_S \times N_{S1}(t) \\ \dfrac{\Delta T}{T}(T_1 - T_n) = -\sigma_T \times N_{T1}(t) \\ \dfrac{\Delta T}{T}(S_0 - S_1) = \sigma_S \times (N_{S0}(0) - N_{S0}(t)) \\ N_{S0}(0) = N_{S0}(t) + N_{S1}(t) + N_{T1}(t) \end{cases}$$

Equation S2

Since the time-dependent spectra for the three transitions are highly overlapped, we treated every spectral region as a mixture of singlet and triplet excitons. Therefore, it takes the form as:

$$\frac{\Delta T}{T}(E,\ t) = (\sigma_{S0}(E,t) - \sigma_{S1}(E,t))N_{S1}(t) + (\sigma_{S0}(E,t) - \sigma_{T1}(E,t))N_{T1}(t)$$

In light of the excitation pulse temporal profile, we used the following fitting function for our data:

$$\frac{\Delta T}{T} = \frac{Erf(c1\times(t-c2))+1}{2} \times c3 \times e^{-k_F t} + c4 \times (1 + \frac{1}{k_F - k_Q}(k_Q e^{-k_F t} - k_F e^{-k_Q t}))$$

Equation S3

where Erf denotes the Gauss error function.

Triplet Davydov Splitting of Pentacene Single Crystals

We performed polarized transient absorption experiments on pentacene single crystals too. Figure S5 shows transient absorption spectra of pentacene single crystals at a time delay of 4 ps with probes along the long *a*-axis and the short *b*-axis when a 400-nm photoexcitation is applied along the *b*-axis. The $T_1 \rightarrow T_n$ transitions exhibit different absorption peaks at 608 nm and 618 nm along the long *a*- axis and short *b*-axis, respectively. The triplet Davydov splitting results show that the triplet energy level along the *b*-axis is higher than that along the *a*-axis, i.e., $E_{T_{1b}+T_{1b}} > E_{T_{1a}+T_{1a}}$.

Technical Details of Quantum Mechanics/Molecular Mechanics Simulations

In our hybrid quantum mechanics/molecular mechanics (QM/MM) study, density functional theory (DFT)(Hohenberg et al., 1964) was employed to accurately model the singlet fission process within a hexacene tetramer, which was selected to span along the ***a*** and ***b*** crystal axes. In addition, all nearest-neighboring molecules of the tetramer were also included in the QM subsystem to account for the electronic polarization effect. By contrast, generalized AMBER empirical force field (GAFF)(Wang et al., 2004) was used to efficiently describe the thermal fluctuation of other hexacene molecules consisting of the MM subsystem. Unless other specified, all QM/MM simulations were performed using CP2K package(VandeVondele et al., 2005) with Goedecker-Teter-Hutter (GTH) pseudopotential,(Goedecker et al., 1996) optimally tuned range-separated hybrid Perdew-Burke-Ernzerhof (ω-RSH-PBE) exchange-correlation functional,(Jacquemin et al., 2014) polarized-valence-double-ζ (PVDZ) basis set,(Woon et al., 1994) electrostatic QM/MM coupling scheme,(Laino et al., 2005) and a wavelet-based Poisson solver.(Genovese et al., 2006)

Simulated Formation Rate of Correlated Triplet Pair

As shown in Table S1, the optical gap for the $S_0S_0 \rightarrow S_0S_1^*$ transition along ***a*** axis is 1.65 eV, which is 0.23 eV higher than its counterpart along ***b*** axis. In spite of their relatively small difference on the optical gap, these two optical transitions have distinct oscillator strengths, i.e., 5.57×10^{-3} vs. 8.94×10^{-3}, making the light absorption along ***b*** axis nearly 60% stronger than that along ***a*** axis. Both of our calculated optical gaps and oscillator strengths are well in line with the experimental absorption spectrum (Figure. 1C).

In our FMSF theory(Elenewski et al., 2017b), the effective vibrational mode that drives singlet fission, is a linear combination of all normal modes, $\vec{V}_{SF} = \sum_i c_i \vec{V}_i$, where c_i reflects the relative importance of the i th normal mode. Mathematically, $\{c_i\}$ can be ascertained by maximizing the Pearson's correlation coefficient between $\{\vec{V}_i\}$ and $\{\Delta E_i^d\}$,(Chen, 2014) where $\Delta E^d = E_{S_0 S_1^*} - E_{TT}$ is the energy gap between $S_0 S_1^*$ and (TT). Specifically, our training set for $\vec{V}_{SF}$ consists of 3,000 snapshots extracted from a 3-ns trajectory of molecular dynamics (MD) simulation. As shown in Figure S8, regardless of the lattice direction of singlet fission, $\vec{V}_{SF}$ is always a ring-stretching mode that is collectively exerted by two adjacent hexacene molecules. Therefore, it is not surprising that the profile of c_i^2 features a few prominent peaks around 1200 cm^{-1} and 1500 cm^{-1}, making the vibrational quantum tunneling effect important for singlet fission since $\hbar\omega_{vib} \gg k_B T$. As a prudent measure to ensure the statistical quality of $\vec{V}_{SF}$, the determined c_i^2 were projected onto another 3000 snapshots extracted from a different MD trajectory for cross validation. It turns out that the cross-validated Pearson's coefficients, $R_C^{aa} = 0.88$ and $R_C^{bb} = 0.88$, are only slightly smaller than their counterparts of the training set $R^{aa} = 0.92$ and $R^{bb} = 0.91$ (Figure S9), suggesting satisfactory sampling for the functional mode analysis of $\vec{V}_{SF}$.

Once the composition of $\vec{V}_{SF}$ is ascertained, we can evaluate its effective angular frequency $\Omega = \sqrt{\frac{\lambda}{\hbar}\sum_{i=1} c_i^2 \omega_i}$ by assuming that the contribution of a given normal mode to

λ is proportional to its relative importance to $\vec{V}_{SF}$. As listed in Table S2, λ along ***a*** axis is 0.46 eV, which is 0.06 eV higher than that along ***b*** axis. The moderate difference on λ can be ascribed to a greater distortion of the hexacene crystal needed to accommodate a longer spin separation distance along ***a*** axis. Nevertheless, Ω_{aa} of 1752 cm^{-1} is even slightly slower than Ω_{bb} of 1902 cm^{-1} due to the higher weights of slower vibrational modes in $\vec{V}_{SF}$ along ***a*** axis (Figure S8). Interestingly, the values of both λ are less than $\left|\Delta G_0\right|$, placing the singlet fission into the inverted Marcus region. The applicability of Marcus-type non-adiabatic transition theory is further justified by our calculated feeble electronic coupling strengths of ~10 meV, which are in line with previous studies on other acenes.(Elenewski et al., 2017a; Yost et al., 2014)

Besides singlet fission, another important decay channel for an optically populated $S_0S_1^*$ vibronic state is its thermal relaxation. According to the phonon scattering theory,(Li et al., 2014) the lifetime of a given vibrational normal mode, $\vec{V}_i$, is decided by its anharmonic coupling with others. If only the third-order anharmonicity is considered, its decay rate, Γ_i is given by:

$$\Gamma_i = \sum_j \sum_k \frac{\hbar\pi\left(f_i + f_k + 1\right)}{4\omega_i\omega_j\omega_k}\left|\frac{\partial^3 E}{\partial\vec{V}_i\partial\vec{V}_j\partial\vec{V}_k}\right|^2 \delta\left(\omega_i - \omega_j - \omega_k\right) \qquad \text{Equation S4}$$

where ω s are the angular frequencies, $f = \frac{1}{e^{\hbar\omega/k_BT} - 1}$ is the Bose-Einstein distribution function, $\frac{\partial^3 E}{\partial\vec{V}_i\partial\vec{V}_j\partial\vec{V}_k}$ is the third-order derivate of energy with respect to all participating

normal modes, and δ is the Dirac delta function. Using the ALAMODE simulation package,(Tadano et al., 2014) the third-order anharmonicity of our system was evaluated through a non-linear least squares regression subject to translational symmetry constraint. Thereafter, Γ_i was calculated by exploring all energy-conversing scattering events. The profile of Γ_i weighted by c_i^2 (Figure S10) again features a couple of distinct peaks at ~1200 cm^{-1} and ~1500 cm^{-1}, further signifying the importance of these ring-stretching normal modes not only to singlet fission but also to thermal relaxation. Now, with all needed parameters in hand, we can apply Eq.2 to calculate k_F under non-thermalized condition. It was found that k_F^{aa} of 0.93 ps^{-1} is nearly same as k_F^{bb} of 0.83 ps^{-1}, in spite of a modest disparity in energetic parameters such as ΔG_0 and λ. The diminished difference on k_F along ***a*** and ***b*** axes primarily arises from their fast Ωs, whose zero-point energies become much more overwhelming for vibrational quantum tunneling. If the fluorescent decay of $S_0S_1^*$ to S_0S_0 is negligible, the overall decay rate, k_D, of $S_0S_1^*$ is simply $k_F + \Gamma$, leading to k_D^{aa} of 1.86 ps^{-1} and k_D^{bb} of 2.08 ps^{-1}.

Derivation of Energy Gap Associated with Quantum Decoherence

Using a two-electron-two-orbital scheme, one can easily construct the three constituent states for a molecule at its triplet state:

$$T_x = \left\{ \begin{array}{c} \left(\begin{array}{c} \uparrow \\ \uparrow \end{array} \right) \begin{array}{l} a \\ b \end{array} \\ \frac{1}{\sqrt{2}} \left(\begin{array}{c} \downarrow \\ \uparrow \end{array} + \begin{array}{c} \uparrow \\ \downarrow \end{array} \right) \\ \left(\begin{array}{c} \downarrow \\ \downarrow \end{array} \right) \end{array} \right. \qquad \text{Equation S5}$$

where we denote the upper and lower orbitals as a and b, respectively. Similarly, we can construct another molecule's triplet state using different upper and lower orbitals denoted as c and d:

$$\left. \begin{array}{c} \begin{array}{l} c \\ d \end{array} \left(\begin{array}{c} \uparrow \\ \uparrow \end{array} \right) \\ \frac{1}{\sqrt{2}} \left(\begin{array}{c} \downarrow \\ \uparrow \end{array} + \begin{array}{c} \uparrow \\ \downarrow \end{array} \right) \\ \left(\begin{array}{c} \downarrow \\ \downarrow \end{array} \right) \end{array} \right\} = T_y \qquad \text{Equation S6}$$

For a fully decoupled $T_x + T_y$ dimer, all nine possible cross-molecule combinations of the constituent states are equally weighted, resulting in an energy expectation value of

$$E_{T_x+T_y} = -k_b T \ln(3\times 3) + E_{coulomb} + E_x^{ab} + E_x^{cd} + \frac{1}{2}\left(E_x^{ac} + E_x^{bc} + E_x^{ad} + E_x^{bd}\right) \qquad \text{Equation S7}$$

where $k_b \ln(3\times 3)$ is the electronic entropy, T is the temperature, $E_{coulomb}$ is the coulomb energy arising from all orbital pairs, and E_x stands form the exchange energy between a selected orbital pair. For example, E_x^{ab} is the exchange energy between orbital a and orbital b.

Alternatively, $E_{T_x+T_y}$ can be expressed as

$$E_{T_x+T_y} = -k_b T \ln 9 + \frac{3}{2} E_{HS} - \frac{1}{2} E_{LS}$$

Equation S8

where E_{HS} and E_{LS} are the energies of the following spin configurations:

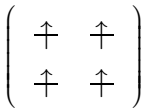 and 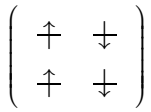 , respectively.

For a $\left(T_x T_y\right)$ pair at its singlet state:

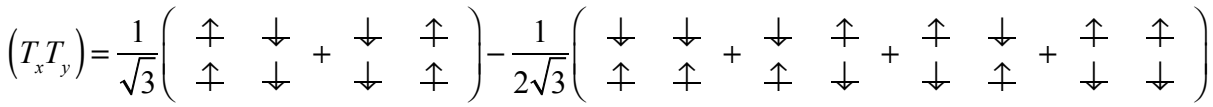

Equation S9

its energy is given by:

$$E_{\left(T_x T_y\right)} = k_b T \ln\left(9\right) + E_{coulomb} + E_x^{ab} + E_x^{cd} - \frac{1}{2}\left(E_x^{ac} + E_x^{bc} + E_x^{ad} + E_x^{bd}\right)$$

Equation S10

which can be further simplified as

$$E_{\left(T_x T_y\right)} = \frac{1}{2} E_{HS} + \frac{1}{2} E_{LS}$$

Equation S11

Through a comparison between Eq. 4 and Eq. 7, we found that

$$\Delta E_{QD} = E_{\left(T_x T_y\right)} - E_{T_x+T_y} = k_b T \ln 9 + E_{LS} - E_{HS} = k_b T \ln 9 + E_{HS \to LS}$$

Equation S12

where $E_{HS\rightarrow LS}$ is the associated spin-flip energy.

Reference

Chen, H., (2014). Functional Mode Electron-Transfer Theory. J. Phys. Chem. C *118*, 7586-7593.

Elenewski, J.E., Cubeta, U.S., Ko, E., Chen, H., (2017a). Computer Simulation of Singlet Fission in Single Crystalline Pentacene by Functional Mode Vibronic Theory. J. Phys. Chem. C *121*, 11159-11165.

Elenewski, J.E., Cubeta, U.S., Ko, E., Chen, H., (2017b). Functional Mode Singlet Fission Theory. J. Phys. Chem. C *121*, 4130-4138.

Genovese, L., Deutsch, T., Neelov, A., Goedecker, S., Beylkin, G., (2006). Efficient solution of Poisson's equation with free boundary conditions. J. Chem. Phys. *125*, 074105.

Goedecker, S., Teter, M., Hutter, J., (1996). Separable dual-space Gaussian pseudopotentials. Phys. Rev. B *54*, 1703-1710.

Hohenberg, P., Kohn, W., (1964). Inhomogeneous Electron Gas. Phys. Rev. *136*, B864-B871.

Jacquemin, D., Moore, B., Planchat, A., Adamo, C., Autschbach, J., (2014). Performance of an Optimally Tuned Range-Separated Hybrid Functional for 0–0 Electronic Excitation Energies. J. Chem. Theory Comput. *10*, 1677-1685.

Laino, T., Mohamed, F., Laio, A., Parrinello, M., (2005). An Efficient Real Space Multigrid QM/MM Electrostatic Coupling. J. Chem. Theory Comput. *1*, 1176-1184.

Laudise, R.A., Kloc, C., Simpkins, P.G., Siegrist, T., (1998). Physical vapor growth of organic semiconductors. J. Cryst. Growth *187*, 449-454.

Li, W., Carrete, J., A. Katcho, N., Mingo, N., (2014). ShengBTE: A solver of the Boltzmann transport equation for phonons. Comput. Phys. Commun. *185*, 1747-1758.

Tadano, T., Gohda, Y., Tsuneyuki, S., (2014). Anharmonic force constants extracted from first-principles molecular dynamics: applications to heat transfer simulations. J. Phys.: Condens. Matter *26*, 225402.

VandeVondele, J., Krack, M., Mohamed, F., Parrinello, M., Chassaing, T., Hutter, J., (2005). Quickstep: Fast and accurate density functional calculations using a mixed Gaussian and plane waves approach. Comput. Phys. Commun. *167*, 103-128.

Wang, J., Wolf, R.M., Caldwell, J.W., Kollman, P.A., Case, D.A., (2004). Development and testing of a general amber force field. J. Comput. Chem. *25*, 1157-1174.

Watanabe, M., Chang, Y.J., Liu, S.-W., Chao, T.-H., Goto, K., Islam, M.M., Yuan, C.-H., Tao, Y.-T. *et. al.*, (2012). The synthesis, crystal structure and charge-transport properties of hexacene. Nat. Chem. *4*, 574-578.

Woon, D.E., Jr., T.H.D., (1994). Gaussian basis sets for use in correlated molecular calculations. IV. Calculation of static electrical response properties. J. Chem. Phys. *100*, 2975-2988.

Yost, S.R., Lee, J., Wilson, M.W.B., Wu, T., McMahon, D.P., Parkhurst, R.R., Thompson, N.J., Congreve, D.N. *et. al.*, (2014). A transferable model for singlet-fission kinetics. Nat. Chem. *6*, 492-497.